Princeton Plasma Physics Laboratory

PPPL- 4780

PPPL- 4780

Paraxial WKB Method Applied to the Lower Hybrid Wave Propagation

N. Bertelli, O. Maj, E. Poli, R. Harvey, J.C. Wright, P.T. Bonoli,
C.K. Phillips, A.P. Simov, E. Valeo and J.R. Wilson

July, 2012

Prepared for the U.S. Department of Energy under Contract DE-AC02-09CH11466.

Princeton Plasma Physics Laboratory
Report Disclaimers

Full Legal Disclaimer

Trademark Disclaimer

PPPL Report Availability

Princeton Plasma Physics Laboratory:

http://www.pppl.gov/techreports.cfm

Office of Scientific and Technical Information (OSTI):

http://www.osti.gov/bridge

Related Links:

U.S. Department of Energy

Office of Scientific and Technical Information

Fusion Links

Paraxial WKB method applied to the lower hybrid wave propagation[a)]

N. Bertelli,[1, b)] O. Maj,[2] E. Poli,[2] R. Harvey,[3] J. C. Wright,[4] P. T. Bonoli,[4] C. K. Phillips,[1] A. P. Smirnov,[5] E. Valeo,[1] and J. R. Wilson[1]

[1)] *Princeton Plasma Physics Laboratory, Princeton, NJ 08543, USA*

[2)] *Max-Planck-Institut für Plasmaphysik, EURATOM Association, Garching, Germany*

[3)] *CompX, Del Mar, CA 92014, USA*

[4)] *MIT Plasma Science and Fusion Center, Cambridge, Massachusetts 02139, USA*

[5)] *Lomonosov Moscow State University, Moscow, Russia*

(Dated: 29 June 2012)

The paraxial WKB (pWKB) approximation, also called beam tracing method, has been employed in order to study the propagation of lower hybrid (LH) waves in a tokamak plasma. Analogous to the well-know ray tracing method, this approach reduces Maxwell's equations to a set of ordinary differential equations, while, in addition, retains the effects of the finite beam cross-section, and, thus, the effects of diffraction.

A new code, `LHBEAM` (Lower Hybrid BEAM tracing), is presented, which solves the pWKB equations in tokamak geometry for arbitrary launching conditions and for analytic and experimental plasma equilibria. In addition, `LHBEAM` includes linear electron Landau damping for the evaluation of the absorbed power density and the reconstruction of the wave electric field in both the physical and Fourier space. Illustrative `LHBEAM` calculations are presented along with a comparison with the ray tracing code `GENRAY` and the full wave solver `TORIC-LH`.

[a)] This article is dedicated to the memory of Grigory Pereverzev.

[b)] nbertell@pppl.gov

I. INTRODUCTION AND BACKGROUND

Lower hybrid current drive (LHCD) is an efficient tool for non-inductively driving current off-axis in tokamak plasmas. Hence, it may play an important role for the current profile control in the advanced tokamak scenario[1]. Some unresolved issues in the study of the LH wave propagation still exist, such as the spectral gap problem[2], i.e., the fact that the parallel (to the magnetic field) refractive index spectrum generated at the plasma edge does not appear to be wide enough to allow the waves to interact with a large number of electrons, and the most recent one related to the "density limit" in the efficiency of LHCD[3,4].

The most common approach employed to analyze radio-frequency wave propagation, and specifically LH wave propagation, is the ray tracing (RT) method based on the WKB approximation, also known as the geometrical optics method[5–9]. For the specific case of high frequency wave beams in stationary media, this approach is based on the fact that the typical inhomogeneity scale of the plasma L is much larger than the radiation wavelength λ. This is referred to as the short-wavelength limit and can be expressed by the introduction of a large dimensionless parameter

$$\kappa \equiv \frac{\omega L}{c} = k_0 L \gg 1, \tag{1}$$

(where c is the speed of light, $\omega = 2\pi f$, with f the wave frequency, and $k_0 \equiv \omega/c$ is the wave vector in free space). In the geometrical optics approach, the relevant solution of Maxwell's equations is approximated by the corresponding asymptotic solution in the limit $\kappa \to +\infty$, which is constructed by tracing a bundle of propagation paths (rays), each one being independent of the others and carrying a specific phase, refractive index vector, amplitude and polarization. Geometrical optics provides a very powerful tool for solving Maxwell's equations in the short-wavelength limit, since it provides a simple picture (in terms of rays) of the wave propagation and a direct application to practical problems. In fact, the integration of the set of ordinary differential equations for the ray bundle is, from a computational point of view, straightforward and cheap. Although geometrical optics is widely employed in literature, it is important to remark that condition (1) gives a necessary but not a sufficient condition for its validity[9,10]. There are situations in which the applicability of geometrical optics is violated, even if the short-wavelength condition (1) is fulfilled: this is typically the case for LH waves, which are considered in this work. The necessary and sufficient conditions for the applicability of geometrical optics have been analyzed in detail

by Kravtsov and Orlov[9]: the validity of the geometrical optics approximation is essentially related to diffraction effects. Roughly speaking, a sufficient condition (Fresnel condition) for the applicability of the geometrical optics for a focused/collimated beam is[9]

$$\frac{W^2}{\ell} \geq \lambda \tag{2}$$

where W is the width of the beam cross-section, and ℓ is the length of the propagation path. In other words, condition (2) states that if $W \geq \sqrt{\lambda\ell}$, diffraction does not play a significant role; on the other hand, if $W \leq \sqrt{\lambda\ell}$, diffraction must be taken into account.

Condition (2) shows that a new scale length comes explicitly into play, namely, the beam width W. In practice, the length of the propagation path is assumed to be $\ell = \mathcal{O}(L)$, hence, diffraction effects are significant for

$$\frac{W}{L} = \mathcal{O}\left(\frac{1}{\sqrt{\kappa}}\right). \tag{3}$$

This last ordering is the basis of the paraxial WKB (pWKB) approximation, also called beam tracing method, which is addressed in this work. In particular, this approach allows one to derive a set of ordinary differential equations as in geometrical optics, taking into account diffraction effects[11–13] (see Section II). Techniques other than the pWKB approximation, such as the parabolic wave equation[14–18] and the quasi-optics approximation[19–23], which address asymptotic solutions of Maxwell's equations in the same regime (3), have also been considered in literature. With respect to the pWKB approximation, those other methods rely either on a set of partial differential equations (PDE)[14–18] or on constrained ordinary differential equations (ODE)[19–23], the solution of which is, in general, computationally more demanding. As mentioned above, the propagation of LH wave beams is one case in which the sufficient condition (2), for the application of geometrical optics, can be violated[24,25]. In other words, diffraction effects are expected to play a significant role in the propagation of LH waves as shown in the work of Pereverzev[26].

Moreover, LH wave beams in the multi-pass regime[27] undergo a series of reflections from cut-offs and caustics singularities that are difficult to describe within the framework of high frequency asymptotics, even for beam tracing and other advanced methods. These kind of limitations motivated the development of direct numerical solutions of Maxwell's equations, which have recently been made available by full wave solvers such as the `TORIC-LH`[28] and the `LHEAF`[29] codes. As the name suggests, full wave codes are capable of following the beam,

in principle, without limitations. Asymptotic methods and full wave solvers are complementary tools: on one hand, asymptotic methods lead to extremely fast and lightweight codes with a clear interpretation of results; on the other hand, full wave solvers, despite being computationally demanding, account for all the details in the propagation, and can guide the further development of asymptotic methods.

The aim of this paper is to show the application of the pWKB approximation to LH wave propagation by using a new code, called `LHBEAM`, which has all numerical advantages of the most common ray tracing method and, at the same time, takes into account diffraction phenomena. Preliminary results have been shown in Refs. 30, 31. In addition to the LH beam propagation, the evaluation of the absorbed power density through linear electron Landau damping and the reconstruction of the electric field are included in `LHBEAM` and they are discussed here for the first time. This paper is structured as follows: the pWKB approximation is reviewed in Section II. In Section III, a description of the `LHBEAM` code is presented. Numerical results are shown in Section IV. Some examples of LH beam propagation and power density profiles obtained by `LHBEAM` with different central electron temperature are shown together with a comparison with the ray tracing code `GENRAY`[32] and the full wave solver `TORIC-LH` for both a circular cross-section equilibrium and an Alcator C-Mod like equilibrium.

II. PARAXIAL WKB METHOD

In this section, the pWKB equations for an electromagnetic wave beam, with a Gaussian profile, propagating in stationary and spatially non-dispersive media are reviewed and a few comments are given on their physical meaning. The formal derivation of these equations is based on the works of Pereverzev[11,12] and Poli et al.[13].

The pWKB method accounts for the detailed form of the wave field by retaining the diffractive pattern of the beam cross-section, which is characterized by the intermediate scalelength W (see equation (3)). Specifically, the ordering in half-integer powers of $1/\kappa$ implied by equation (3) is employed to perform an expansion (*paraxial expansion*) around the beam axis (also called reference ray). In physical terms, the wave field is supposed to be localized around the reference ray, i.e., the wave field is exponentially small as $\kappa \to +\infty$, away from it. It is therefore enough to compute all physical quantities in a neighborhood of

size $W = \mathcal{O}\left(1/\sqrt{\kappa}\right)$ of the reference ray.

The pWKB method provides a solution of Maxwell's electromagnetic wave equation

$$\nabla \times \nabla \times \mathbf{E} - k_0^2 \boldsymbol{\varepsilon} \cdot \mathbf{E} = 0, \tag{4}$$

(where $\boldsymbol{\varepsilon}$ is the cold plasma dielectric tensor) in the form

$$\mathbf{E}(\mathbf{r}) = A(\mathbf{r})\mathbf{e}(\mathbf{r})e^{ik_0\bar{s}(\mathbf{r})} = A(\mathbf{r})\mathbf{e}(\mathbf{r})e^{ik_0[s(\mathbf{r})+i\phi(\mathbf{r})]}, \tag{5}$$

where $A(\mathbf{r})$ and $\mathbf{e}(\mathbf{r})$ are the wave amplitude and the polarization unit vector, respectively, while, the function $\bar{s}(\mathbf{r}) = s(\mathbf{r}) + i\phi(\mathbf{r})$ is the *complex* eikonal.

According to the discussion above, the functions $A(\mathbf{r})$, $\mathbf{e}(\mathbf{r})$, $s(\mathbf{r})$ and $\phi(\mathbf{r})$ are given by their Taylor expansion around the reference ray up to the appropriate order, namely (summation over repeated indices is adopted)

$$A(\mathbf{r}) = A_0(\tau), \quad \mathbf{e}(\mathbf{r}) = \mathbf{e}_0(\tau), \tag{6}$$

$$\begin{aligned} s(\mathbf{r}) &= s_0(\tau) + N_i(\tau)[x^i - x^i(\tau)] \\ &+ \frac{1}{2} s_{ij}(\tau)[x^i - x^i(\tau)][x^j - x^j(\tau)], \end{aligned} \tag{7}$$

$$\phi(\mathbf{r}) = \frac{1}{2}\phi_{ij}(\tau)[x^i - x^i(\tau)][x^j - x^j(\tau)], \tag{8}$$

where $\mathbf{r} = (x^i)$, while $x^i(\tau)$ and $N_i(\tau)$ are the coordinates and the components of the refractive index $\mathbf{N} = c\mathbf{k}/\omega$ along the reference ray, respectively. Here, $\tau = \tau(\mathbf{r})$ is the value of the parameter along the reference ray, for which the vector $(x^i - x^i(\tau))$ belongs to the prescribed beam cross-section passing through $(x^i(\tau))$. Typically, for electromagnetic waves, this corresponds to the value of τ, for which $(x^i - x^i(\tau))$ is orthogonal to the reference ray. For LH waves, however, the beam tends to line up with the equilibrium magnetic field, hence, it is convenient to make use of poloidal sections of the tokamak to define beam cross-sections, i.e., $\tau(\mathbf{r})$ is chosen so that $(x^i - x^i(\tau))$ belongs to the poloidal section passing through $(x^i(\tau))$. Let us recall that different choices of the beam cross-sections yield the same solution within an $\mathcal{O}\left(1/\sqrt{\kappa}\right)$ error, which is the order of the error of the pWKB asymptotic solution (5). It is worth noting that, in the expansion of $\phi(\mathbf{r})$, the first two terms are equal to zero because, $\phi(\mathbf{r})$, evaluated on the reference ray, is zero by construction and, being, in addition, positive-definite, we also have $\nabla\phi = 0$ (for all details the reader is referred to Refs. 11-13). Then, $x^i(\tau)$ and $N_i(\tau)$ satisfy the set of Hamiltonian differential equations of ray

tracing,

$$\frac{dx^i}{d\tau} = \frac{\partial H}{\partial N_i}, \quad \frac{dN_i}{d\tau} = -\frac{\partial H}{\partial x^i}, \tag{9}$$

where H is the (real) determinant of the dispersion tensor $\mathbf{\Lambda} = (\mathbf{NN} - N^2\mathbf{I}) + \boldsymbol{\varepsilon}^h$ with $\mathbf{N}(\equiv c\mathbf{k}/\omega)$ the refractive index, $\mathbf{I}$ the identity tensor and $\boldsymbol{\varepsilon}^h$ the Hermitian part of the plasma dielectric tensor. Correspondingly, $s_0(\tau) = \int^\tau \mathbf{N} \cdot d\mathbf{r}(\tau')$. The remaining functions s_{ij} and ϕ_{ij} obey the equations

$$\begin{aligned}\frac{ds_{ij}}{d\tau} = &- \frac{\partial^2 H}{\partial x^i \partial x^j} - \frac{\partial^2 H}{\partial x^j \partial N_k} s_{ik} - \frac{\partial^2 H}{\partial x^i \partial N_k} s_{jk} \\ &- \frac{\partial^2 H}{\partial N_k \partial N_l} s_{ik} s_{jl} + \frac{\partial^2 H}{\partial N_k \partial N_l} \phi_{ik} \phi_{jl},\end{aligned} \tag{10}$$

$$\begin{aligned}\frac{d\phi_{ij}}{d\tau} = &- \left(\frac{\partial^2 H}{\partial x^i \partial N_k} + \frac{\partial^2 H}{\partial N_k \partial N_l} s_{il} \right) \phi_{jk} \\ &- \left(\frac{\partial^2 H}{\partial x^j \partial N_k} + \frac{\partial^2 H}{\partial N_k \partial N_l} s_{jl} \right) \phi_{ik}.\end{aligned} \tag{11}$$

The solution of these equations is subject to both the dispersion equation $H = 0$ on the reference ray, and the constraints

$$\frac{\partial H}{\partial x^i} + s_{ij} \frac{\partial H}{\partial N_j} = 0, \tag{12}$$

$$\phi_{ij} \frac{\partial H}{\partial N_j} = 0, \tag{13}$$

the derivatives of H being also evaluated on the reference ray. Hence, the number of independent equations, for s_{ij} and ϕ_{ij}, is reduced to six. In particular, equations (12) and (13) can be employed either to reduce the number of equations or as a check of the numerical accuracy. Diffraction effects are found as a result of the coupling between equation (10) for s_{ij} and (11) for ϕ_{ij}.

In order to understand the physical meaning of s_{ij} and ϕ_{ij}, we consider a simple case in which the beam propagates in free space along the x-direction and both s_{ij}, ϕ_{ij} are diagonal. Then, equations (12) and (13) give the constraints $s_{xx} = 0$ and $\phi_{xx} = 0$, respectively. In this particular situation we can set $\tau(\mathbf{r}) = x$, and the wave electric field, given by equation (5), becomes (dropping the amplitude and the polarization)

$$\begin{aligned}\mathbf{E} \propto \quad &\exp\left\{ ik_0 \left[s_0(x) + \frac{1}{2} \left(s_{yy}(x) y^2 + s_{zz}(x) z^2 \right) \right] \right. \\ &\left. - \frac{k_0}{2} \left[\phi_{yy}(x) y^2 + \phi_{zz} z^2 \right] \right\},\end{aligned} \tag{14}$$

where $s_0(x) = \int^x N_x(x')dx'$ describes the phase evolution on the reference ray (i.e., along the propagation direction) and has the same physical meaning as in geometrical optics. The next step is to introduce the radii of curvature of the phase front R_α and the beam widths W_α, in such a way that the quadratic terms, present in equation (14), can be written in a form which clarifies their physical interpretation

$$s_{\alpha\alpha}(x) \equiv \frac{1}{R_\alpha(x)}, \quad \text{(no sum over } \alpha\text{)}, \tag{15}$$

and

$$\phi_{\alpha\alpha}(x) \equiv \frac{2/k_0}{W_\alpha^2(x)}, \quad \text{(no sum over } \alpha\text{)}, \tag{16}$$

for $\alpha = y$ or $\alpha = z$. Therefore, the symmetric matrix s_{ij} is connected with the curvature of the wave front, whereas ϕ_{ij} describes the beam profile. In addition, from equation (14), one can note that the contour levels of the amplitude profile in the y-z plane are determined by a quadratic form whose axes are aligned with the y and z axes of the laboratory system. Such a quadratic form $\phi_{yy}y^2 + \phi_{zz}z^2$ is positive definite and its contour levels are ellipses (they can become circles when two beam widths are the same along the two directions). The ellipse having semi-axes equal to W_α will be called *attenuation* ellipse. An analogous analysis can be carried out for phase fronts that, in particular, are characterized by the quadratic form $s_{yy}y^2 + s_{zz}z^2$ (not necessarily positive definite). When $\phi_{yz} \neq 0$ ($s_{yz} \neq 0$), one has the rotation of the principal widths (the principal radii of curvature) with respect to the fixed reference frame. For instance, in the case of inhomogeneous media, during the propagation of the wave beam, the evolution of the attenuation ellipse can be quite complicated. In fact the attenuation ellipse can rotate and change its eccentricity. In Section IV A, a 3D plot of a LH beam is shown in which the evolution of this attenuation ellipse can be clearly seen.

Analogous to geometrical optics, the amplitude of the wave field is determined by the wave energy transport equation[33],

$$\nabla \cdot (\mathbf{v}_g U) = -2\gamma U, \tag{17}$$

which, in the framework of the pWKB method, is evaluated on the reference ray. Here, $\mathbf{v}_g \left(\propto \mathbf{V} \equiv \frac{\partial H}{\partial \mathbf{N}}\right)$ is the group velocity, $U \propto |A|^2$ is the wave energy density, and $\gamma = |\partial H/\partial\omega|^{-1}\, \mathbf{e}^* \cdot \boldsymbol{\varepsilon}^a \cdot \mathbf{e}$ is the absorption coefficient ($\boldsymbol{\varepsilon}^a$ is the anti-Hermitian part of the dielectric tensor). In addition, the polarization vector $\mathbf{e}$ is obtained, as in geometrical optics, by the equation $\boldsymbol{\Lambda} \cdot \mathbf{e} = 0$ also evaluated on the reference ray. It is important to stress that,

although the wave energy transport equation (17) is formally the same as the corresponding geometrical optics equation, the group velocity is different. More specifically, the effects of diffraction enter equation (17) through the term

$$\nabla \cdot \mathbf{V} = \frac{\partial}{\partial x^i}\frac{\partial H}{\partial N_i} + \frac{\partial^2 s}{\partial x^i \partial x^j}\frac{\partial^2 H}{\partial N_i \partial N_j}, \tag{18}$$

in which the dependence on the matrix $\partial^2 s/\partial x^i \partial x^j = s_{ij}$ is evident, and this quantity is coupled to the beam widths as discussed above. For the specific case of an isotropic medium, the analysis of such a contribution has been carried out in Ref. 34.

The pWKB equations (9)-(11) constitute a system of ordinary differential equations[11,12,35], for which an initial value problem is posed. In particular, the relevant quantities for the initial conditions are the launching position, the components of the refractive index (consistently with the dispersion relation) on the beam axis, the quadratic forms s_{ij} and ϕ_{ij} (consistently with the constraints) related to the phase front and the principal widths of the attenuation ellipse, respectively. Further comments about this will be given in Section IV A.

III. CODE DESCRIPTION

`LHBEAM`, Fortan 90 code for LH waves, is derived from the `TORBEAM` code, which is the first implementation of the pWKB equations for Gaussian wave beams with frequencies in the electron-cyclotron frequency range in fusion plasmas[35]. The aim of `LHBEAM` is to solve numerically the 20 ordinary differential equations of the pWKB approximation, in particular, the equations for the reference ray (cf. equations (9)), the equations for the components of the symmetric matrices s_{ij}, ϕ_{ij} (cf. equations (10), (11)) and the equations for the wave amplitude and the power (cf. equation (17)), in the lower hybrid range of frequency. The dispersion equation $H = 0$, which in the pWKB approximation holds on the reference ray only, and the six constraints (cf. equations (12),(13)) are used to prescribe consistent initial conditions for the beam parameters and, during the run, as a check of accuracy. With reference to equations (9)-(13), in the `LHBEAM` code the dispersion function H can be chosen to be either the full electromagnetic dispersion function

$$\begin{aligned} H_{ELM} = S\, N_\perp^4 - \left[\left(S - N_\parallel^2\right)(P+S) - D^2\right] N_\perp^2 \\ + P\left[\left(S - N_\parallel^2\right)^2 - D^2\right], \end{aligned} \tag{19}$$

or the electrostatic dispersion function

$$H_{ELS} = SN_{\perp}^2 + PN_{\parallel}^2, \tag{20}$$

where $N_\perp$ ($N_\parallel$) is the perpendicular (parallel) component of the refractive index with respect to magnetic field. Here, the plasma dielectric tensor is computed in the cold plasma limit, and in the range of LH frequency, for which, $\omega_{ci}^2 \ll \omega^2 \ll \omega_{ce}^2$. In particular, the elements of the cold dielectric tensor are[36]

$$S = 1 + \frac{\omega_{pe}^2}{\omega_{ce}^2} - \frac{\omega_{pi}^2}{\omega^2}, \;\; D = \frac{\omega_{pe}^2}{\omega\omega_{ce}}, \;\; P = 1 - \frac{\omega_{pe}^2}{\omega^2} - \frac{\omega_{pi}^2}{\omega^2}, \tag{21}$$

where

$$\omega_{\rm pe}^2(\mathbf{r}) \equiv \frac{4\pi n_e(\mathbf{r}) e^2}{m_{\rm e}}, \quad \omega_{\rm ce}(\mathbf{r}) \equiv \frac{eB(\mathbf{r})}{m_{\rm e}c}, \tag{22}$$

and

$$\omega_{\rm pi}^2(\mathbf{r}) \equiv \sum_{\rm i=species} \frac{4\pi n_i(\mathbf{r}) Z_{\rm i} e^2}{m_{\rm i}} \approx \frac{4\pi n_e(\mathbf{r}) Z_{\rm eff} e^2}{m_{\rm main}}, \tag{23}$$

are the square of the electron plasma frequency, the electron cyclotron frequency and the square of the ion plasma frequency, respectively ($n_{\rm e}$ ($n_{\rm i}$) is the electron (ion) density, e the absolute value of the electron charge, and $m_{\rm e}$ ($m_{\rm i}$) the electron (ion) mass, $\mathbf{B}$ the confinement magnetic field, $Z_{\rm eff}$ the effective charge of the plasma, and $m_{\rm main}$ the mass of the main ion species). In the case of full electromagnetic dispersion function, equation (19) is just the determinant of the dispersion tensor, i.e., no mode selection is operated at this level. With this choice, the derivatives of H can be calculated in a simpler way. The slow wave mode (corresponding to the LH waves) is selected by imposing appropriate initial conditions.

Regarding the evaluation of the power absorption of LH waves, in `LHBEAM` a Maxwellian plasma is considered. Therefore the main contribution of the imaginary part of the dispersion relation corresponds to linear electron Landau damping. More specifically, the absorbed power is calculated according to the equation

$$\frac{dP}{d\tau} = -2\alpha_{\rm ELD} \left| \frac{\partial H}{\partial \mathbf{N}} \right| P, \quad \frac{d}{d\tau} \equiv \frac{\partial H}{\partial \mathbf{N}} \cdot \frac{\partial}{\partial \mathbf{r}}, \tag{24}$$

which follows from equation (17) by integrating in flux tube of the group velocity. Here,

α_{ELD} corresponds to the linear electron Landau damping given by[37–39]

$$\alpha_{\mathrm{ELD}} = \frac{\gamma}{|\mathbf{v}_{\mathrm{g}}|} = 2\sqrt{\pi}\left(\frac{\omega_{\mathrm{pe}}}{\omega}\right)^2 \frac{\omega}{c}\frac{c^3}{N_\parallel^3 v_{\mathrm{th}}^3} \times \left[(S - N_\parallel^2)(S - N^2) - D^2\right] \times \left|\frac{\partial H}{\partial \mathbf{N}}\right|^{-1} \exp\left[-\frac{c^2}{v_{\mathrm{th}}^2 N_\parallel^2}\right]. \tag{25}$$

In equation (25), $v_{\mathrm{th}} \equiv \sqrt{2T_{\mathrm{e}}/m_{\mathrm{e}}}$ is the electron thermal velocity.

The plasma equilibrium can be prescribed either analytically or from experimental data. In the former case, an analytical representation of the poloidal and toroidal components of the magnetic field is implemented taking into account the Shafranov shift and the elongation of the plasma (see Ref. 35). The radial profile of the density and the temperature are given in the following form

$$f(r) = (f_0 - f_{\mathrm{edg}})\left[1 - \left(\frac{r}{a}\right)^{e_1}\right]^{e_2} + f_{\mathrm{edg}} \tag{26}$$

where $f(r)$ stands for both the density ($n(r)$) and the temperature ($T(r)$) and the subscripts "0" and "edg" refer the values at the plasma core ($r = 0$) and plasma edge ($r = a$), respectively. In equation (26), a is the minor radius of the plasma torus and f_0, f_{edg}, e_1 and e_2 are given as input parameters for both density and temperature. In the experimental case, the magnetic configuration is provided numerically by assigning the (Cartesian) components of the static magnetic field $\mathbf{B}$ and a flux coordinate ψ on a grid in the poloidal plane (x, z). Density and temperature are also prescribed numerically. They are given as functions of ψ.

IV. RESULTS AND BENCHMARK

In this section, results for the beam trajectory, the evolution of the refractive index throughout the propagation and the power deposition profile obtained from `LHBEAM` are compared with the ray tracing code `GENRAY`[32] and the full wave solver `TORIC-LH`[28].

A. Numerical results

The tokamak plasma equilibrium adopted in this subsection has a circular cross-section with a major radius $R_0 = 64$ cm and a minor radius $a = 16.5$ cm. The magnetic field is $B(R_0) = 8$ T and the plasma current is $I_{\mathrm{p}} = 400$ kA. The magnetic equilibrium is

provided by a data file generated by the ACCOME code[40]. Temperature and density profiles are parabolic following equation (26), with the central and the edge electron density given by $n_{e,0} = 5 \times 10^{19}$ m^{-3} and $n_{e,edg} = 1 \times 10^{19}$ m^{-3}. Three different values for the central electron temperature, $T_{e,0} = 3, 5, 10$ keV are considered, with the same edge electron temperature, $T_{e,edg} = 0.5$ keV, for all three cases. Plasma parameters mentioned here are based on the Alcator C experiment[41,42]. Regarding the initial conditions of the LH wave beam, a precise matching of the pWKB solution (5) to the electric field generated at the antenna mouth is beyond the scope of this work. Initial conditions are given in the natural form for the system of first-order ordinary differential equations (9)-(11) and (24). One prescribes the initial position $(x_0^i) = (80.2, 0, 0)$ in cm, already in the propagation region inside the plasma (LH waves are evanescent at the antenna mouth), together with the parallel refractive index $N_{\parallel,0} = 2.5$ (on the beam axis), which, assuming that the poloidal component of $\mathbf{N}$ is zero (on beam axis), and using the dispersion relation at the initial point, is enough to determine the other components of $\mathbf{N}$ in the laboratory frame. The quadratic forms s_{ij} and ϕ_{ij} in the initial point are chosen so that the initial phase front is flat, cf. equation (15), and the attenuation ellipse is vertical with half-height $W_1 = 2.7$ cm, in order to match to a single waveguide height, and width $W_2 = 0.4$ cm (here, W_1 and W_2 refer to the principal widths of the attenuation ellipse (cf. equation (16))). The input power is assumed to be 1 MW and the full electromagnetic dispersion function (cf. equation (19)) is adopted. The frequency of LH beam is 4.6 GHz.

Figure 1 shows a 3D propagation of the LH wave beam for $T_{e,0} = 5$ keV launched in the equatorial plane. In Figure 1, the evolution of the attenuation ellipse mentioned in Section II is plotted (blue lines) showing its rotation during the LH beam propagation. The beam axis trajectory is also plotted (in red). A zoom-in of Figure 1(a) from another point of view is shown in Figure 1(b). Here, in addition to the evolution of the attenuation ellipse, the direction of the wave vector is also shown along the beam axis, represented by the (green) arrows pointing to the high field side, together with the direction of the magnetic field, represented by the (black) arrows pointing basically in the opposite directions to the trajectory of the beam. This figure emphasizes clearly one of the main feature of LH waves: they tend to propagate parallel to the magnetic field (although, in this specific case, in the opposite direction), while the wave vector tends to be perpendicular to the static magnetic field. Though it is not immediately evident from figure 1(b) that the LH

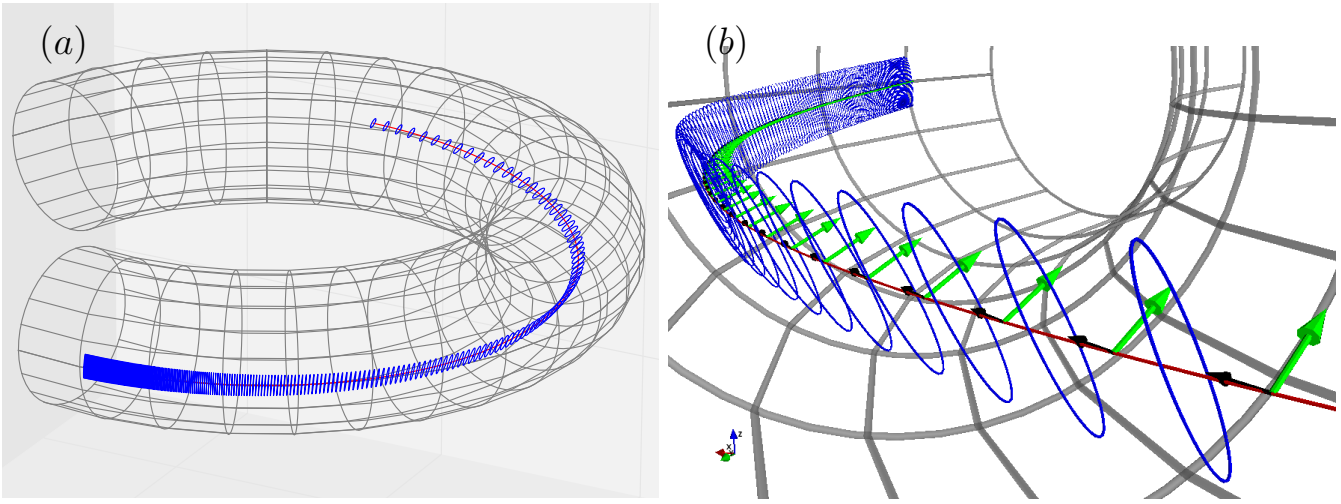

FIG. 1. (a) 3D evolution of the LH wave beam for $T_{e,0} = 5$ keV and $N_{\|,0} = 2.5$. Attenuation ellipses (mentioned in Section II) are plotted (in blue), together with the beam axis (in red). (b) A zoom-in of figure (a) from another point of view. The large (green) arrows represent the wave vector direction along the LH propagation pointing to the high field side, while the small (black) arrows represent the direction of the magnetic field opposite to the direction of the LH wave beam.

wave is a backward wave, the projection of the wave vector onto the beam axis, which corresponds to the direction of the group velocity, is indeed negative, although small. In order to illustrate the effects of the diffraction on the LH wave beam propagation, Figure 2 shows a comparison between the poloidal projection of the wave beam propagation obtained from `LHBEAM`, represented by the shaded area (which corresponds to the projections of the attenuation ellipses on the poloidal plane), with the poloidal projection of a bundle of rays generated by the ray tracing code `GENRAY`, represented by the dashed lines. As in Figure 1, the solid (red) line refers to the beam axis. The difference between the two approaches is evident: in particular, the spatial wave beam broadening originated by diffraction effects is very significant and completely missing in the ray tracing description. This situation appears to be typical: the size of the bundle of geometrical optics rays underestimates the beam width (see also Refs. 26, 30). It is worth recalling that `LHBEAM` solves the pWKB equations for a cold plasma (here, also `GENRAY` makes use of a cold plasma model), therefore the wave beam trajectory and rays are independent of the temperature. Any changes in the temperature affect only the location of the absorbed power deposition along the wave beam. Figure 2 shows the positions along the wave beam at which the power is fully absorbed for

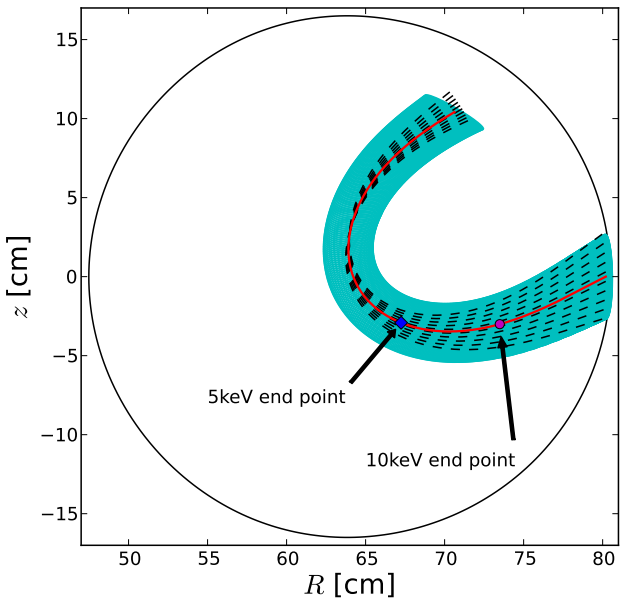

FIG. 2. Comparison between pWKB and ray tracing methods for the LH wave propagation in the poloidal cross-section. The colored area represents the projections of the attenuation ellipses on the poloidal section obtained from `LHBEAM` and the solid (red) curve is the beam axis, whereas the dashed (black) curves represent 10 rays generated by `GENRAY`. The solid (blue) diamond and the solid (magenta) circle indicate the position along the wave beam in which the power is fully absorbed, respectively, for $T_\mathrm{e} = 5$ keV and 10 keV.

$T_{\mathrm{e},0} = 5$ keV (shown with a solid (blue) diamond) and 10 keV (shown with a solid (red) circle). For the lower temperature of 3 keV the beam is not fully absorbed in the first pass.

Another feature of `LHBEAM` is the possibility of a simple reconstruction of the wave electric field, following equation (5). In the pWKB method, the solution for the wave field is directly obtained in the physical space, as opposed to Fourier space, which is exploited by spectral full wave solvers. In order to represent the wave electric field in the same way as a spectral full wave solver, like `TORIC-LH`, which typically considers only a single wave toroidal mode number n_φ, we have performed a Fourier transform in the toroidal angle φ of the electric field (which in the pWKB framework takes into account also the toroidal width of the antenna in a natural way). The result is the wave electric field $\mathbf{E}(R, z, n_\varphi)$, spectrally resolved in the toroidal mode number n_φ, and expressed as a function of (R, z) in the poloidal plane. A numerical result of this procedure is shown in Figure 3, for the magnitude of the parallel

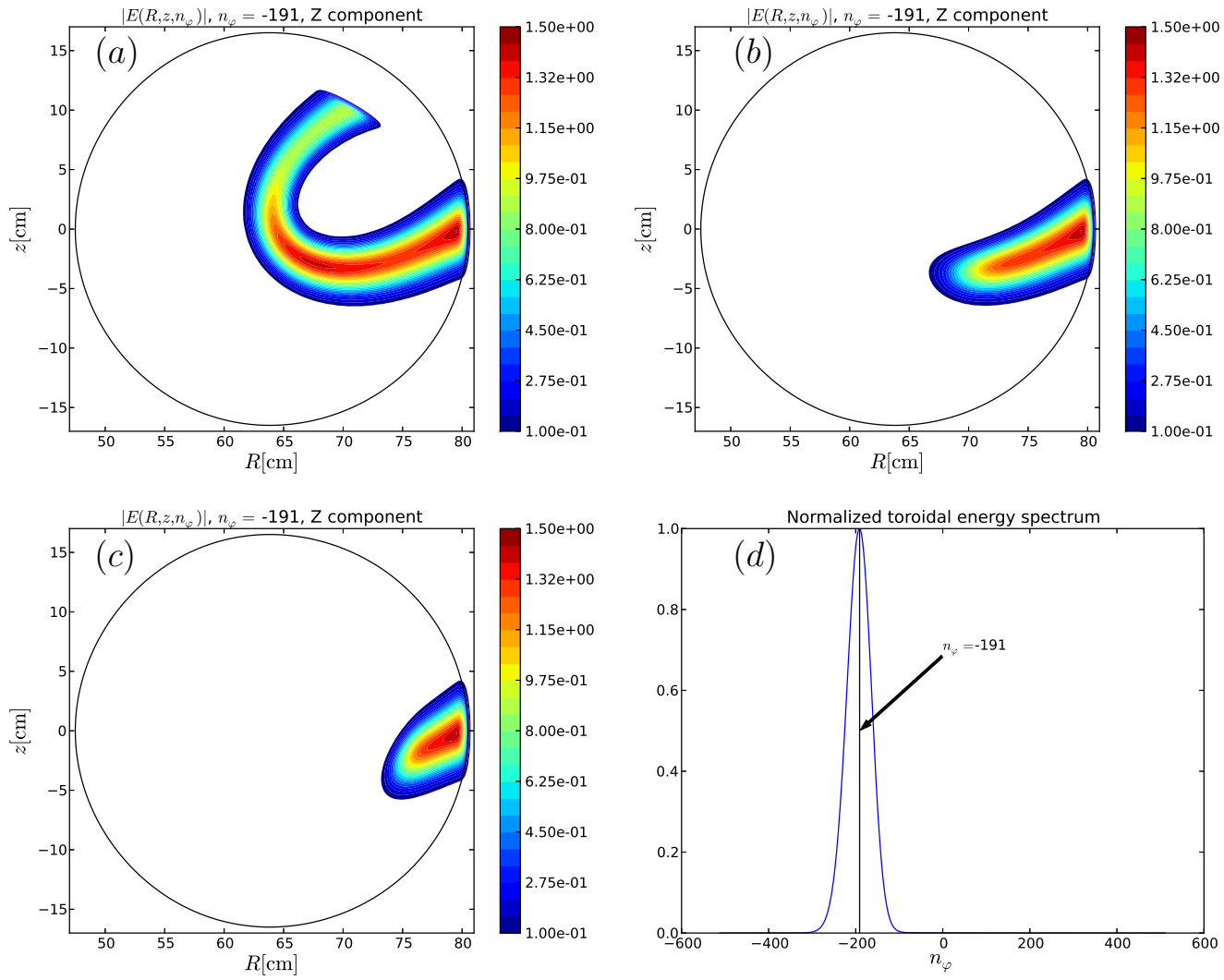

FIG. 3. Magnitude of the parallel component of the complex electric field normalized to its value at the launching point of the reference ray for three different cases: $T_{e,0} = 3$ keV (figure (a)), 5 keV (figure (b)), 10 keV (figure (c)), for the fixed toroidal mode number $n_\varphi = -191$, which corresponds to the dominant component of the spectrum, showing in figure (d).

(with respect to the magnetic field) component of the complex electric field (normalized to the value of the total electric field amplitude at the launching point of the reference ray) for $T_{e,0} = 3$ keV (figure 3(a)), $T_{e,0} = 5$ keV (figure 3(b)) and $T_{e,0} = 10$ keV (figure 3(c)), all for the value of $n_\varphi = -191$, which corresponds to the toroidal mode that carries the maximum energy. This is shown in figure 3(d), where the electric field energy $\int |\mathbf{E}(R, z, n_\varphi)|^2 R\mathrm{d}R\mathrm{d}z$ carried by each n_φ mode is plotted (normalized to its maximum). The dominant component

of the n_φ-spectrum, namely, $n_\varphi = -191$, is found to be slightly different in comparison with the input parameter $n_\varphi = -196$ for the corresponding run of TORIC-LH. This is due to (i) small differences in the initial conditions in LHBEAM as compared to the boundary conditions in TORIC-LH; (ii) the numerical tolerances of the discrete Fourier transform of the wave field (which has been computed with 1024 uniformly distributed sample points in φ). Comparing Figure 2 with Figure 3, one can see that the parallel component of the electric field follows very well the beam trajectory and that its maximum lies on the beam axis and decreases away from it. This feature could be useful for the interpretation of results generally obtained from full wave solvers where it is much more complicated to distinguish the evolution of the parallel electric field along the beam trajectory. In addition, the positions along the wave beam at which the power is fully absorbed (shown in Figure 2 by the solid (blue) diamond and the solid (magenta) circle for $T_\mathrm{e} = 5$ keV and 10 keV, respectively) are in good agreement with the contour levels of the parallel electric field shown in Figure 3. One can also note that the magnitude of the parallel electric field close to the launching point has a similar behavior for all three cases considered. In fact, the 3 keV case seems to be an extension of the 5 keV and 10 keV cases.

It is important to mention that the current version of LHBEAM does not deal with caustic singularities and reflection at the plasma edge since that would have required a specific treatment within the framework of the pWKB technique. Further comments about this will be given in the following subsection and in the last section.

B. Benchmark with GENRAY and TORIC-LH

In order to validate the pWKB code for LH waves, LHBEAM is compared to results from other independent codes. A careful comparison of different codes is no easy task, in particular, when each code is based on a different physical model and different kind of approximations. Here, a code validation is presented regarding the trajectory of the propagation and the evolution of the parallel and perpendicular components of the refractive index with the ray tracing code GENRAY[32] and absorbed power with both GENRAY and the full wave solver TORIC-LH[28]. As mentioned in the previous section, the beam axis obeys the ray tracing equations (cf. equations (9)). Therefore, we can compare directly the trajectory of the beam axis calculated by LHBEAM with the trajectory of a single ray calculated by the ray

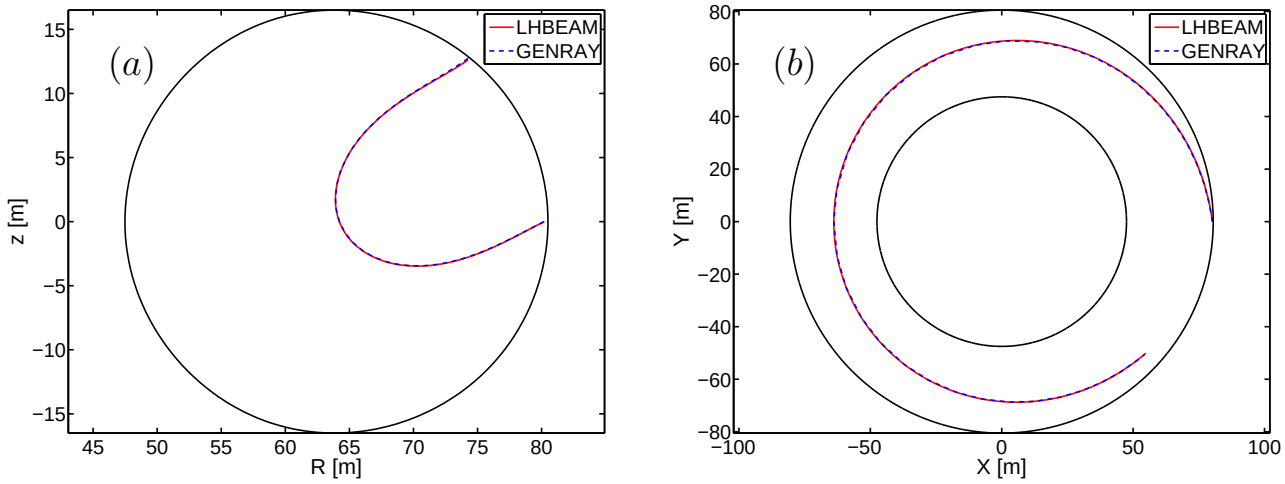

FIG. 4. Poloidal (a) and toroidal (b) projection of the trajectory of the LH beam axis calculated by `LHBEAM` (full red curve) and the trajectory of a single ray calculated by `GENRAY`[32] (dashed blue curve). Circular cross-section equilibrium, parabolic plasma profiles and the initial value of $N_{\|} = 2.5$ and electron temperature $T_e = 3$ keV are assumed.

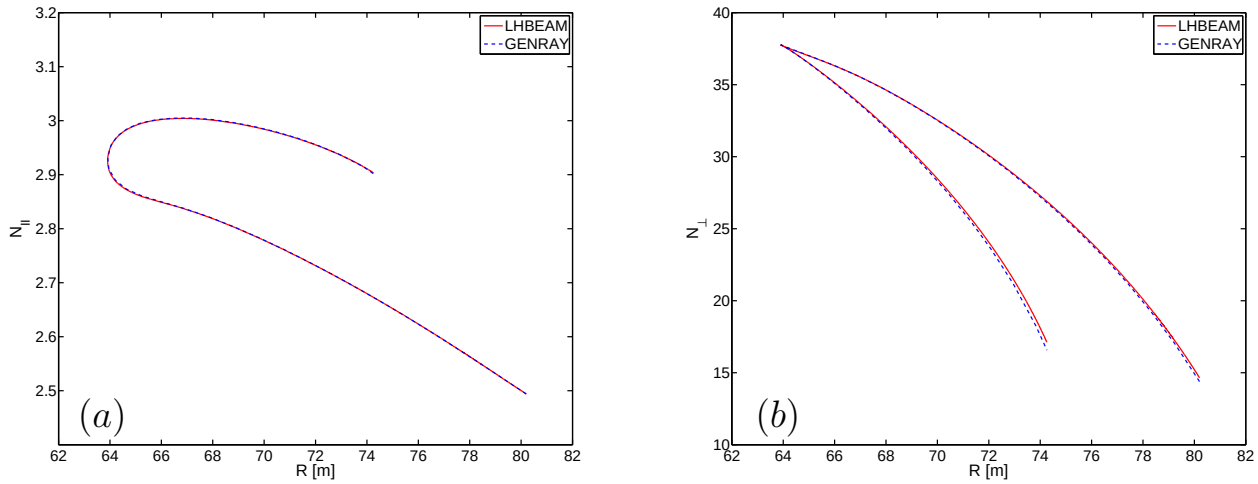

FIG. 5. Parallel (a) and perpendicular (b) component of the refractive index as a function of R, corresponding to the case of Figure 4, calculated by `LHBEAM` (full red curve) and `GENRAY`[32] (dashed blue curve).

tracing code `GENRAY` together with the evolution of the refractive index along the beam axis. (A preliminary code validation has been done in a previous work[31] by using an analytical equilibrium with the ray tracing code `C3PO`[43,44].) Here, we present two cases, one using the

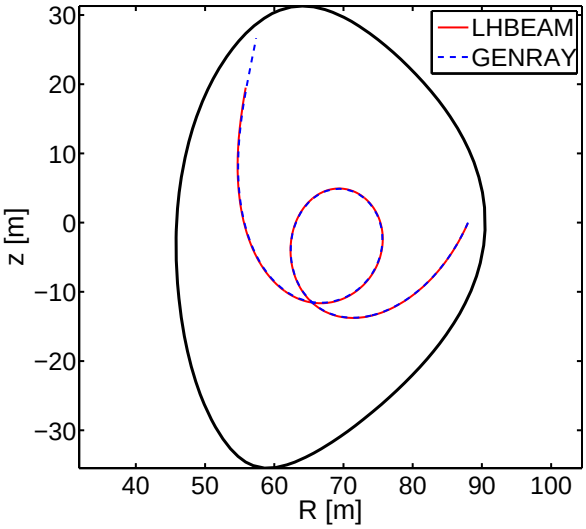

FIG. 6. Poloidal projection of the trajectory of the LH beam axis calculated by LHBEAM (full red curve) and the trajectory of a single ray calculated by GENRAY[32] (dashed blue curve). Alcator C-Mod like equilibrium and the initial value of $N_{\|} = 5$ are assumed.

circular cross-section equilibrium discussed in the previous subsection and one based on an Alcator C-Mod like equilibrium. Figure 4 shows the poloidal (Figure 4(a)) and toroidal (Figure 4(b)) projections of the beam axis obtained by LHBEAM, solid (red) curve, together with the trajectory of a single ray calculated by GENRAY, dashed (blue) curve, assuming $N_{\|,0} = 2.5$ and parabolic plasma profiles with $T_{e,0} = 3$ keV. Excellent agreement between the beam axis and the ray path is found between these two independent codes, in fact, differences between the two curves are hardly noticeable. The same agreement is also seen in Figure 5, where the parallel (Figure 5(a)) and perpendicular (Figure 5(b)) components (with respect to the magnetic field) of the refractive index as a function of the major radius, R, are plotted, respectively. For the Alcator C-Mod like equilibrium, the same good agreement appears in Figures 6 and 7, where again the beam axis trajectory and the evolution of the refractive index (parallel and perpendicular components) are plotted. Therefore, we can conclude that LHBEAM and GENRAY are in remarkable agreement with regard to the trajectory and the evolution of the refractive index during the beam propagation, despite the use of two different interpolation methods for the experimental equilibrium data. Finally, in order to further increase our confidence in the LHBEAM calculations, an additional comparison regarding the power density profile is shown in Figure 8. Figure 8 shows the power density as a function of

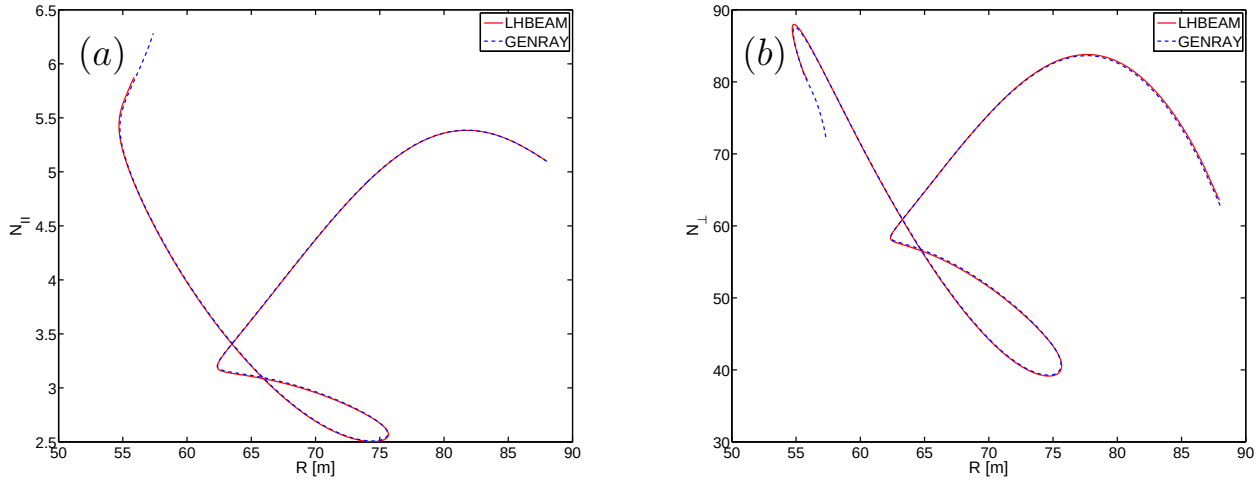

FIG. 7. Parallel (a) and perpendicular (b) component of the refractive index as a function of R, corresponding to the case of Figure 6, calculated by `LHBEAM` (full red curve) and `GENRAY`[32] (dashed blue curve).

the square root of the normalized poloidal flux, ρ_ψ obtained from `LHBEAM`, `GENRAY`, and the full wave code `TORIC-LH`. Three cases are shown for different central electron temperature, namely, $T_{e,0} = 3$ keV (red curves), $T_{e,0} = 5$ keV (green curves) and $T_{e,0} = 10$ keV (black curves) by using circular cross-section equilibrium and parabolic profiles described above. Solid, dashed and dashed-dotted lines correspond to `LHBEAM`, `TORIC-LH` and `GENRAY` results, respectively. From Figure 8, the three considered codes appear to be in good agreement for $T_{e,0} = 5, 10$ keV. Some differences are noted for the $T_{e,0} = 3$ keV case, for which the single-pass absorption is weaker. Since reflections at the plasma edge are not yet included in `LHBEAM`, $T_e = 3$ keV corresponds to a limit case for `LHBEAM`. Nevertheless, the agreement between the pWKB approximation and the full wave approach is quite good. The slight differences between `LHBEAM` and `TORIC-LH` are possibly due to the missing small amount of absorbed power after the reflection of the LH wave beam at the plasma edge that is not included in the `LHBEAM` power deposition profile. The differences with `GENRAY` can be explained by missing full wave effects in the ray tracing model, such as diffraction. This is clearly shown in Figure 2(a) where the pWKB technique shows a significant spatial broadening with respect to the ray tracing method (see also Refs. 26, 30). However, for the strong absorption regime, the location of the peak of the power density and its profiles are in very good agreement among codes, particularly, for $T_{e,0} = 5$ keV and 10 keV. Indeed, such a good

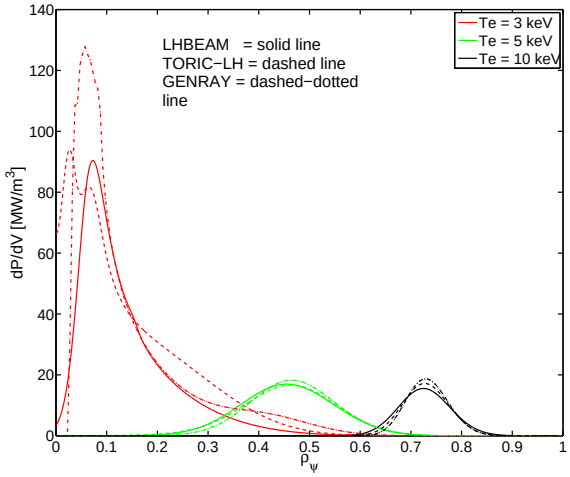

FIG. 8. Power absorption profile as a function of the square root of the normalized poloidal flux, ρ_ψ as calcluated by single-pass `LHBEAM` (solide lines), `GENRAY` (dashed-dotted lines) and `TORIC-LH` (dashed lines) for $T_{e,0} = 3$ keV (red curves), 5 keV (green curves) and 10 keV (black curves). Input power is 1 MW. Note that `LHBEAM` takes into account the full toroidal spectrum.

agreement deserve to be further commented on as the ray tracing, beam tracing and full wave correspond to a rather different description of the wave field. One should first recall that full wave effects (diffraction, in particular) can change the wave energy density distribution in both the physical and Fourier spaces. Ray tracing calculations are not sensitive at all to those effects, which, on the other hand, are captured by a full wave solver. The agreement between `GENRAY` and `TORIC-LH` seems to imply that such effects do not play a significant role in the strong absorption scenarios ($T_{e,0} = 5, 10$ keV), at least, for the cases considered here. However, they are important in the weak absorption case ($T_{e,0} = 3$ keV). The pWKB implementation of `LHBEAM` stands in between: wave effects are fully accounted for in the description of the propagation, but they are only partially accounted for in the description of power deposition. As mentioned in Section II, the wave energy transport equation has been evaluated on the reference ray, and that is rigorously justified only for a spatially non-dispersive medium[11,12]. The electron Landau damping is spatially dispersive, cf. equation (25), and the effects of the finite width of the $N_\parallel$-spectrum should be properly dealt with. The current version of `LHBEAM` does not yet include a proper description of caustic structures and reflections of the beam at the plasma edge. In the limit case of 3 keV, the differences with respect to `GENRAY` profiles can be explained as the effect of both

the diffractive broadening of the beam cross-section (cf. Figure 2(a)) and the missing power after the reflection of the beam. One can also conclude that the effects of the finite width of the $N_\parallel$-spectrum are crucial for the correct description of the LH power deposition in the weak absorption regime.

V. SUMMARY AND DISCUSSION

In this paper, the pWKB method is applied to the LH wave propagation. A description of `LHBEAM`, a pWKB code for Gaussian beams of LH waves, has been provided, and the possibility of the 3D reconstruction of the LH wave field has been demonstrated. Unlike the electric field obtained from a full wave solver, which typically makes use of a single toroidal mode number, the electric field based on the pWKB approximation takes into account, in a natural way, the whole n_φ-spectrum. In other words, the finite size of the antenna, not only in the poloidal but also in the toroidal direction are included in the beam description. The dominant n_φ mode can easily be singled out by a discrete Fourier transform, leading to results close to full wave calculations, cf. Figure 3. Comparison of the propagation of the LH wave beam described by `LHBEAM` and the bundle of rays obtained from `GENRAY` demonstrated that the spatial wave beam broadening caused by diffraction effects, which is completely missing in the ray tracing description, is captured by pWKB method, and can be very significant.

A detailed validation of `LHBEAM` has been also presented. A comparison of the trajectory of the beam axis and the evolution of the refractive index with ray paths from `GENRAY`, has been analyzed for both a circular equilibrium with parabolic plasma profiles and an Alcator C-Mod like equilibrium and plasma profiles. Excellent agreement in both cases is found. In addition, a comparison of the power deposition profile from `LHBEAM` with results from `GENRAY` and the full wave solver `TORIC-LH` has been studied. Good agreement has been found in strong absorption regimes (also called the single-pass absorption regime). However, in the weak absorption limit, some differences are found, in part because `LHBEAM` does not include the cut-offs and reflections. A specific analysis and treatment in the pWKB framework is required to include these effects. For the very strong absorption cases ($T_{\mathrm{e},0} = 5, 10$ keV analyzed in the previous section), the results obtained from pWKB approximation, ray tracing and full wave approach are very similar, suggesting that, at least in the considered

cases, diffraction effects are not so significant for the calculations of the absorbed power. In a weaker absorption regime ($T_{e,0} = 3$ keV), the pWKB seems to be more accurate than the ray tracing method, despite the lack of reflection treatment in the current version of `LHBEAM`. This is, in fact, a promising result. Still it remains to investigate the effect of spectral broadening in the absorbed power due to diffraction effects in the weak absorption regime together with a specific treatment of the caustics and cut-offs, which are expected to be important for an accurate modeling of the multi-pass regime. These topics will be addressed in a future work.

In summary, the agreement between `LHBEAM` and `TORIC-LH` presented in this work , in the moderate and strong absorption regimes, suggests that the pWKB technique can capture part of the physics described by full wave solvers and, therefore, help to extract physical insight from them. As discussed above, work is underway to extend the pWKB method to the weak damping regime. It is important, in fact, to mention that the application of the pWKB technique requires much less computation time and resources with respect to the full wave approach. This would provide an accurate reduced model that executes much faster than the full wave LH propagation and absorption calculations.

ACKNOWLEDGMENTS

The many insightful discussions with M. Bornatici, R. Bilato and M. Brambilla are gratefully acknowledged. This research is supported by the U.S. Department of Energy under contract number DE-FC02-99ER54512.

REFERENCES

[1]C. Gormezano and et al, Nucl. Fusion **47**, S285 (2007).

[2]P. T. Bonoli and R. C. Englade, Phys. Fluids **29**, 2937 (1986).

[3]G. Wallace and et al, Phys. Plasmas **17**, 082508 (2010).

[4]R. Cesario and et al, Plasma Phys. Control. Fusion **53**, 085011 (2011).

[5]S. Weinberg, Phys. Rew. **126**, 1899 (1962).

[6]L. D. Landau and E. M. Lifshitz, *The Classical Theory of Fields* (Pergamon Press, Oxford, 1987).

[7]I. B. Bernstein, Phys. Fluids **18**, 320 (1975).

[8]M. Brambilla and A. Cardinali, Plasma Physics **24**, 1187 (1982).

[9]Y. A. Kravtsov and Y. I. Orlov, *Geometrical Optics of Inhomogeneous Media*, Vol. 6 (Springer Series on Wave Phenomena, 1990).

[10]Y. A. Kravtsov and Y. I. Orlov, Sov. Phys. Usp. **23**, 750 (1980).

[11]G. V. Pereverzev, *Reviews of Plasma Physics*, edited by B. B. Kadomtsev, Vol. 19 (1996).

[12]G. V. Pereverzev, Phys. Plasmas **5**, 3529 (1998).

[13]E. Poli, G. V. Pereverzev, and A. G. Peeters, Phys. Plasmas **6**, 5 (1999).

[14]V. A. Fock, *Electromagnetic Diffraction and Propagation Problems* (Pergamon Press, New York, 1965).

[15]G. V. Permitin and A. I. Smirnov, JETP **82**, 395 (1996).

[16]A. I. Smirnov and E. Y. Petrov, in *Proceedings of the 26th EPS Conference on Plasma Physics and Controlled Fusion*, Vol. 23J (1999) p. 1797.

[17]A. A. Balakin, M. A. Balakina, G. V. Permitin, and A. I. Smirnov, J. Phys. D: Appl. Phys. **40**, 4285 (2007).

[18]A. A. Balakin, M. A. Balakina, and E. Westerhof, Nucl. Fusion **48**, 065003 (2008).

[19]S. Choudhary and L. B. Felsen, Proc. IEEE Trans. Antennas Propag. **AP-21**, 827 (1973).

[20]E. Mazzucato, Phys. Fluids B **1**, 1855 (1989).

[21]S. Nowak and A. Orefice, Phys. Fluids B **5**, 1945 (1993).

[22]S. Nowak and A. Orefice, Phys. Plasmas **1**, 1242 (1994).

[23]D. Farina, Fusion Sci. and Technol. **52**, 154 (2007).

[24]G. V. Pereverzev, in *20th EPS Conference on Contr. Fusion and Plasma Phys.*, Vol. 17C, Part III (1993) p. 885.

[25]A. Cardinali and et al, Phys. Plasmas **14**, 112506 (2007).

[26]G. V. Pereverzev, Nucl. Fusion **32**, 1091 (1992).

[27]A. S. Richardson, P. T. Bonoli, and J. C. Wright, Phys. Plasmas **17**, 052107 (2010).

[28]J. C. Wright and et al, Phys. Plasmas **16**, 072502 (2009).

[29]O. Meneghini, S. Shiraiwa, and R. Parker, Phys. Plasmas **16**, 090701 (2009).

[30]N. Bertelli and et al, in *34th EPS Conf. on Plasma Phys.*, Vol. 31F (2007) p. P5.051.

[31]N. Bertelli and et al, in *AIP Conference Proceedings*, Vol. 1069 (2008) pp. 259–264.

[32]A. P. Smirnov and R. W. Harvey, in *Bull. Am. Phys. Soc.*, Vol. 40 (1995) p. 1837.

[33]E. Poli and et al, Fusion Engineering and Design **53**, 9 (2001).

[34]M. Bornatici and O. Maj, Plasma Phys. Control. Fusion **45**, 707 (2003).

[35]E. Poli, A. G. Peeters, and G. V. Pereverzev, Comp. Phys. Comm. **136**, 90 (2001).

[36]T. H. Stix, *Waves in Plasmas* (American Institute of Physics, NY, 1992).

[37]P. T. Bonoli, IEEE Trans. on Plasma Science **PS-12**, 95 (1984).

[38]M. Spada and et al, Nucl. Fusion **31**, 447 (1991).

[39]F. Imbeaux and Y. Peysson, Plasma Phys. Control. Fusion **47**, 2041 (2005).

[40]R. S. Devoto and et al, Nucl. Fusion **32**, 773 (1992).

[41]M. Porkolab and et al, Phys. Rev. Lett. **53**, 450 (1984).

[42]M. Porkolab and et al, Phys. Rev. Lett. **53**, 1229 (1984).

[43]Y. Peysson, J. Decker, and V. Basiuk, in *34th EPS Conf. on Plasma Phys.*, Vol. 31F (2007) p. P4.164.

[44]Y. Peysson, J. Decker, and L. Morini, Plasma Phys. Control. Fusion **54**, 045003 (2012).

The Princeton Plasma Physics Laboratory is operated
by Princeton University under contract
with the U.S. Department of Energy.

Information Services
Princeton Plasma Physics Laboratory
P.O. Box 451
Princeton, NJ 08543

Phone: 609-243-2245
Fax: 609-243-2751
e-mail: pppl_info@pppl.gov
Internet Address: http://www.pppl.gov